Journal of Fluids Engineering

Copy of e-mail Notification

Journal of Fluids Engineering Published by ASME

Dear Author,

Congratulations on having your paper accepted for publication in the ASME Journal Program.

Your page proof is available from the ASME Proof site here:

http://115.111.50.156/jw/AuthorProofLogin.aspx?pwd=2ccc86325324&CA=AS

Login: your e-mail address

Password: 2ccc86325324

Please keep this email in case you need to refer back to it in the future.

Responsibility of detecting errors rests with the author. Please review the page proofs carefully and:

1. Answer any queries on the “Author Query Form”
2. Proofread any tables and equations carefully
3. Check to see that any special characters have translated correctly
4. Publication will not proceed until a response is received. If there are no corrections, a response is still required.

RETURNING CORRECTIONS:

Corrections must be returned using the ASME Proof Download & Corrections Submission Site (link above). You will be able to upload:

1. Annotated PDF
2. Text entry of corrections, with line numbers, in the text box provided
3. Additional files, if necessary.

SPECIAL NOTES:

Your Login and Password are valid for a limited time. Please reply within 48 hours.

Corrections not returned through the above website will be subject to publication delays.

This e-proof is to be used only for the purpose of returning corrections to the publisher.

If you have any questions, please contact: asme.cenveo@cenveo.com, and include your article no. (FE-16-1514) in the subject line. This email should not be used to return corrections.

Approval of these proofs re-confirms the copyright agreement provision that all necessary rights from third parties for any copyrighted material (including without limitation any diagrams, photographs, figures or text) contained in the paper has been obtained in writing and that appropriate credit has been included.

Sincerely,

Jim Kennedy, Journal Production Manager

STATEMENT OF EDITORIAL POLICY AND PRACTICE

The Technical Committee on Publications and Communications (TCPC) of ASME aims to maintain a high degree of technical, literary, and typographical excellence in its publications. Primary consideration in conducting the publications is therefore given to the interests of the reader and to safeguarding the prestige of the Society.

To this end the TCPC confidently expects that sponsor groups will subject every paper recommended by them for publication to careful and critical review for the purpose of eliminating and correcting errors and suggesting ways in which the paper may be improved as to clarity and conciseness of expression, accuracy of statement, and omission of unnecessary and irrelevant material. The primary responsibility for the technical quality of the papers rests with the sponsor groups.

In approving a paper for publication, however, the TCPC reserves the right to submit it for further review to competent critics of its own choosing if it feels that this additional precaution is desirable. The TCPC also reserves the right to request revision or condensation of a paper by the author or by the staff for approval by the author. It reserves the right, and charges the editorial staff, to eliminate or modify statements in the paper that appear to be not in good taste and hence likely to offend readers (such as obvious advertising of commercial ventures and products, comments on the intentions, character, or acts of persons and organizations that may be construed as offensive or libelous), and to suggest to authors rephrasing of sentences where this will be in the interest of clarity. Such rephrasing is kept to a minimum.

Inasmuch as specific criteria for the judging of individual cases cannot, in the opinion of the TCPC, be set up in any but the most general rules, the TCPC relies upon the editorial staff to exercise its judgment in making changes in manuscripts, in rearranging and condensing papers, and in making suggestions to authors. The TCPC realizes that the opinions of author and editor may sometimes differ, and hence it is an invariable practice that no paper is published until it has been passed on by the author. For this purpose page proofs of the edited paper are sent to the author prior to publication in a journal. Changes in content and form made in the proofs by authors are followed by the editor except in cases in which the Society's standard spelling and abbreviation forms are affected.

If important differences of opinion arise between author and editor, the points at issue are discussed in correspondence or interview, and if a solution satisfactory to both author and editor is not reached, the matter is laid before the TCPC for adjustment.

Technical Committee on Publications and Communications (TCPC)
Reviewed: 05/2012

AUTHOR QUERY FORM

ASME SETTING THE STANDARD	**Journal: J. Fluids Eng.** **Article Number: FE-16-1514**	**Please provide your responses and any corrections by annotating this PDF and uploading it to ASME's eProof website as detailed in the Welcome email.**

Dear Author,

Below are the queries associated with your article; please answer all of these queries before sending the proof back to Cenveo. Production and publication of your paper will continue after you return corrections or respond that there are no additional corrections.

Location in article	Query / Remark: click on the Q link to navigate to the appropriate spot in the proof. There, insert your comments as a PDF annotation.
AQ1	Reminder – the ASME Copyright Agreement that was signed by all authors includes the following: "You have the right to enter into this Copyright Form and to make the assignment of rights to ASME. If the Paper contains excerpts from other copyrighted material (including without limitation any diagrams, photographs, figures or text), you have acquired in writing all necessary rights from third parties to include those materials in the Paper, and have provided appropriate credit for that third-party material in footnotes or in a bibliography." As required, ASME may contact the authors to obtain a copy of the written permission.
AQ2	Any content obtained from the web and included in the paper may require written permission and appropriate credit if it is copyrighted content. If copyright status cannot be determined, this content should not be included in the paper.
AQ3	Please provide zipcode for all the affiliations.
AQ4	Please provide department details for author "Thomas Duriez."
AQ5	In the sentence beginning "The manuscript…" please specify which section or subsection does "the next section" refers to here.
AQ6	Please define LFD, PMMA and EHD at the first occurrence.
AQ7	Please reword text without color words as readers of print will only see black and white figures.
AQ8	Please check the presentation for Ref. 14.
AQ9	Please provide city name and paper number or page range for Ref. 27.
AQ10	Please provide publisher name and publisher location (city and state/country) for Ref. 49.
AQ11	Please provide publisher location (city and state/country) for Refs. 50 and 51.
AQ12	Please provide DOI or website to access the Refs. 4, 19, 20, 21, 26, 28, 33, 40 and 44.

Thank you for your assistance.

AQ1 AQ3 AQ2

Juan D'Adamo[1]
CONICET,
Facultad de Ingenieria,
Universidad de Buenos Aires,
Buenos Aires ■, Argentina
e-mail: jdadamo@fi.uba.ar

Leandro Leonardo
CONICET,
Facultad de Ingenieria,
Universidad de Buenos Aires,
Buenos Aires ■, Argentina

Federico Castro
CONICET,
Facultad de Ingenieria,
Universidad de Buenos Aires,
Buenos Aires ■, Argentina

Roberto Sosa
CONICET,
Facultad de Ingenieria,
Universidad de Buenos Aires,
Buenos Aires ■, Argentina

AQ4

Thomas Duriez
CONICET,
Facultad de Ingenieria,
Universidad de Buenos Aires,
Buenos Aires ■, Argentina;
■,
Universidad de la Marina Mercante,
Marina Mercante ■, Argentina

Guillermo Artana
CONICET,
Facultad de Ingenieria,
Universidad de Buenos Aires,
Buenos Aires ■, Argentina

Circular Cylinder Drag Reduction By Three-Electrode Plasma Symmetric Forcing

This study reports an efficient reduction of the drag exerted by a flow on a cylinder when the former is forced with a plasma actuator. A three-electrode plasma device (TED) disposed on the surface of the body is considered, and the effect of the actuation frequency and amplitude is studied. Particle image velocimetry measurements provided a detailed information that was processed to obtain the time-averaged drag force and to compare the performances of TED actuator and the canonical dielectric discharge barrier actuator. For the Reynolds number considered (Re = 5500), excitations with the TED actuator were more efficient, achieving drag reductions that attained values close to 40% with high net energy savings. The reduction of coherent structures using the instantaneous vorticity fields and a clustering technique allowed us to gain insight into the physical mechanisms involved in these phenomena. This highlights that the symmetrical forcing of the wake flow at its resonant frequency with the TED promotes symmetrical vorticity patterns which favor drag reductions. [DOI: 10.1115/1.4035947]

1 Introduction

Electrohydrodynamic or plasma actuators have been rapidly developed over the last 20 years in the flow control community. They show unique properties in terms of flow manipulation [1–3] as: (1) momentum addition close to the wall, (2) no moving parts, (3) short command to action delays (of the order of the ms) [4], and (4) high geometric versatility [5], allowing mounting on any surface exposed to the flow. Even though many types of discharge configurations have been proposed over the years (Fig. 1) [6], the acting principle has always been equivalent to the following: (1) the imposed electric field weakly ionizes the air close to the flow-exposed electrode(s), creating a plasma state; (2) the presence of charged particles within the highly nonuniform electric field creates a body force on the fluid near the electrodes' surface through a ion collisional mechanism; and (3) the process is accompanied by a slight heating of the air that locally modifies mass density and viscosity of the fluid.

The different discharge configurations ultimately determine the stability of the discharge, the electrode degradation, the electric force distribution, or the energy consumption required to attain a given air flow.

The most popular of these devices, the dielectric barrier discharge (DBD) actuator (Fig. 1(*b*)), has been used to achieve control of diverse flows [2,3,7], exhibiting strong advantages: a simple implementation, reproducible performances, and relative robustness. It has been successfully applied in many recent engineering problems such as: control of transition [8]; separation of flows for canonical geometries [9] or turbomachines [10], flow control on airfoils for lift augmentation [11], or to enhance their maneuvering [12]; also recently DBD has been used in hybrid

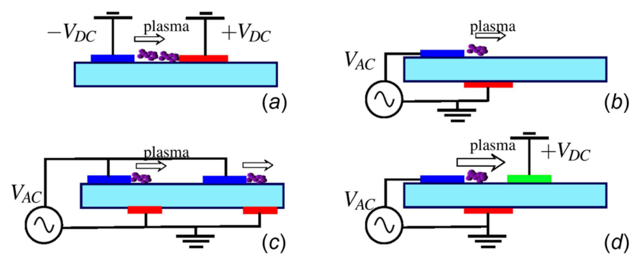

Fig. 1 Different implementations of plasma discharge devices: (*a*) sliding discharge, (*b*) dielectric barrier discharge, (*c*) serial DBD, and (*d*) three electrode discharge

[1]Correspondence author.

Contributed by the Fluids Engineering Division of ASME for publication in the Journal of Fluids Engineering. Manuscript received August 14, 2016; final manuscript received January 23, 2017; published online xx xx, xxxx. Assoc. Editor: Shizhi Qian.

systems of control for a 3D complex geometry [13]. In particular, the flow around a cylinder is a common benchmark to study wake flows and to evaluate active control characteristics: (1) the absolute instability and its small receptivity to extrinsic perturbations ensures the high portability of the results, (2) this flow counts with an extended flow control bibliography, and an already consequent one using plasma actuators [5,14–21], (3) the high-induced momentum by TED can be a key enabler in frustrating the Bénard–von Kármán (BvK) instability. In Ref. [17], the authors performed an interesting survey of the DBD actuator to modify drag and lift forces. They have found important energy savings related to drag reduction and claimed that these could be improved through optimization of the actuator design and the high voltage power-supply.

However, some drawbacks that are inherent to DBD actuators can be mentioned: (1) the wetting of electrodes largely alters the discharge and the actuator performance; (2) the device is sensitive also to other environment conditions such as atmospheric pressure, temperature, and air humidity that modify the dielectric properties of the fluid (breakdown voltage, onset, …) and therefore actuator performance; (3) the high voltage and high frequencies required to operate the device induce high electromagnetic noise that might disturb or damage neighboring electronic systems; (4) as byproduct of the discharge dangerous/polluting species such as O_3 are produced; (5) many applications, such as aeronautics, still require to enhance the momentum added by the actuators as the induced air velocities is limited to a few m/s; (6) the forces produced by a DBD actuator in a flow take place only near the air-exposed electrode and are localized to a few millimeters in a region with a size similar to the region with visible ionization. Considering this size fixed, scale problems in real size applications may arise when extrapolating results of reduced scale models undertaken in a laboratory environment. Additionally, the control of flow separation with DBD is effective when the actuation is produced close to the separation line. Nonetheless, this line may change its position, and the control, therefore, becomes less effective.

In order to mitigate the last two problems one strategy is to extend the ionization region or to enlarge the drift regions of ions. This would increase the induced force and also give a larger versatility to the actuator. With this goal, one proposition has been to place series of DBD actuator disposed along the streamwise direction (multistep DBD, Fig. 1(*c*)) [22]. Some drawbacks of this configuration related to dead zones of actuation have been signaled in the previous studies [23]. A second proposition, investigated by the seminal work of Louste et al. [24] is to modify the electric field configuration and thus the discharge characteristics including a third electrode (TED, Fig. 1(*d*)). Different variations to the initial configuration proposed in Ref. [24] have been proposed over time [25–27].

While DBD and other blowing actuators have actually a limitation concerning the position where momentum is introduced, with TED actuators this position can be enlarged adjusting DC voltage between electrodes [28]. Notably, in the case of wake flow control, TED may provide a dynamically adaptable configuration with respect to the separation line position that depends, for instance, on the Reynolds number.

Concerning wake flow, in Sosa et al. [26], the TED actuator has been tested in continuous blowing mode for the flow around a cylinder with the objective to reduce the drag force. The main findings for the Reynolds numbers considered (8000–10,000) were that the TED actuator achieved higher drag reductions compared to a DBD actuator with the same electrical power consumption.

In the present study, the characterization of the TED actuator is continued using a larger parametric study, including periodic forcing, in order to energetically optimize the control. Drag forces and the recurrent states of the flow can be inferred from flow fields obtained by means of particle image velocimetry (PIV). Access to vorticity dynamics and reduction of coherent structures is achieved through a clustering technique [29].

The manuscript is organized as follows: in the next section the experimental setup is detailed; in Sec. 3, the TED actuator parametric study is described, and raw results are presented; drag forces and power consumption estimated from PIV measurements are shown on Sec. 4; in Sec. 5 drag reductions are discussed by means of global mode analysis and a clustering of the instantaneous flow vorticity fields; finally, conclusions on the link between drag measurements and the inferred wake dynamics are presented in Sec. 6 relating drag measurements to forced wake dynamics.

2 Experimental Setup

The experiments were conducted in the Tango wind tunnel of the LFD [19]. The test section of this facility is of 0.5×0.5 m^2, and the flow velocity during experiments was set to $U_0 = 3.30$ ms^{-1}. The wake flow was generated with a smooth cylinder of external diameter $D = 25 \times 10^{-3}$ m, and length $L = 0.5$ m. As the ratio of the width of the test section with the cylinder diameter was 20 any blockage effect can be neglected. The incoming free stream flow (U_0) had fluctuations around the mean value of $\pm 2\%\, U_0$. The associated Reynolds number was of $\mathrm{Re} = U_0 D/\nu \simeq 5500$ (assuming a kinematic viscosity $\nu = 1.5 \times 10^{-5}$). Considering that a wake flow with this Reynolds number has a typical value of Strouhal number $\mathrm{St} = f_n D/U_0 \simeq 0.2$, the expected natural vortex shedding frequency is $f_n \simeq 26$ Hz. According to the classification of Ref. [30], this cylinder wake flow belongs to the so-called shear layer transition regime.

A 2D PIV acquisition system was used to obtain the two-component flow fields at the midspan of the cylinder (Fig. 2). Hardware and software implementations used in our experiments are similar than those referenced in Ref. [19]. The field of view of the experiment was of 130 mm $\times$ 90 mm (about $8D \times 6D$). During postprocessing of the images with the PIV algorithm, this region was divided into interrogation cells of 16×16 pixels^2 with an overlapping of 50% giving a spatial resolution of the vector fields of $0.06D$. The maximum sampling frequency of the system is about $f_S = 14.8$ Hz, and as this value is lower than the expected shedding frequency f_n, the flow dynamics was subsampled on time. Each test was undertaken with an acquisition of 510 successive snapshots. Assuming ergodicity, the time average velocity fields $\langle \mathbf{u}(\mathbf{x}) \rangle$ and fluctuations of the j velocity component $\langle u'_j(\mathbf{x}) \rangle$ were determined, respectively, as

$$\langle \mathbf{u}(\mathbf{x}) \rangle = \frac{1}{N} \sum_{i=1}^{N} \mathbf{u}(\mathbf{x}, t_i) \qquad (1)$$

$$\langle u'_j(\mathbf{x}) \rangle = \frac{1}{N} \left[\sum_{i=1}^{N} \Big(u_j(\mathbf{x}, t_i) - \langle u_j \rangle \Big)^2 \right]^{(1/2)} \qquad (2)$$

We consider a plasma actuator that has been named previously as three-electrode-discharge (TED) device. Earlier studies with this kind of actuators can be found in Refs. [24,28], and [31]. As the name suggests, TED is made of three electrodes as illustrated in the scheme of Fig. 3(*a*). Electrode *A* is flush mounted and exposed to the air; electrode *B* is encapsulated by a dielectric material. Both electrodes are separated by the 3 mm thick cylindrical wall made of PMMA. The downstream edges of electrode *A* are placed at $\theta = \pm 80$ deg measured from the upstream stagnation point. The third electrode is placed downstream at the symmetry plane of the flow. The distance separating the edges of electrode *A* from the edges of electrode C is 20 mm.

Two configurations are possible with this electrode setup. The first one is quite similar to a classical dielectric barrier discharge (DBD), as in this configuration electrodes B and C are grounded, while the electrode A is energized with a high voltage signal V_{AC}. This high voltage signal is produced with a signal generator, an audio amplifier, an ignition coil, and a high voltage power source (see Ref. [2] for more references). The frequencies and peak to

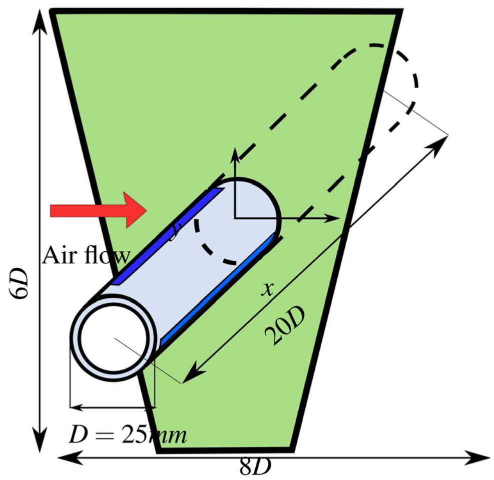

Fig. 2 Scheme of the region analyzed with PIV

peak voltages were fixed at 9 kHz and 11 kV. The position of the DBD discharge is similar to the position considered in other previous studies of wake flow control [5,17,26].

In the second configuration (TED), the electrodes B and C are also grounded, the electrode A is also excited with an AC high voltage signal but, additionally, a direct current negative high voltage is applied to electrode A producing a negative offset of the voltage reference of this electrode. The peak to peak voltage and frequency of the AC high voltage signal were the same as the DBD tests, and the DC signal was varied within the range $V_{\mathrm{DC}} \in [-6 \cdots -11]$ kV. Beyond 11 kV, arc type discharges appears disrupting the electrical stability of the system that could damage the equipment.

In both configurations, burst modulations of the sinusoidal high voltage signal could be performed as illustrated by Fig. 3(*b*). The forcing frequency associated with such modulation of period T_{Burst} is $f_f = 1/T_{\mathrm{Burst}}$. It is convenient to refer this frequency to the natural vortex shedding, and thus, we define the nondimensional frequency $f^+ = f_f/f_n$. In this work, we have explored nondimensional frequencies lying in the range $f^+ \in [0.1 \ldots 5]$. The burst modulation allows to introduce a duty-cycle for the signal, DC%, defined as: $100 \times (T_{\mathrm{On}}/T_{\mathrm{Burst}})$, with T_{On} the time during which the electrodes are energized. This parameter quantifies the fraction of time in which the discharge, and consequently, the forcing is active during one cycle. Higher values of DC produce an increase of the time during which the discharge is ignited and therefore of the time-averaged forcing.

The intensity of actuation depends on the electrical power supplied to the system and the efficiency of the system to transform the electrical energy to mechanical energy. To quantify the electrical power, we measured the electric currents $I_B(t)$ and $I_C(t)$ with shunt resistances ($R = 50\,\Omega$) connected to an oscilloscope. The voltage applied to electrode A was measured with a high voltage, high frequency measurement probe.

There exist other configurations of TED devices that have been reported in the previous works [26–28]. When the electrode C is connected to a high voltage negative DC and electrode A to AC voltage, the discharge has been named sliding discharge, and the ionizatzion of air is visible in all the space between electrodes A and C. When the electrode C is connected to a high voltage positive DC, the discharge has been named enhanced DBD. This last configuration is equivalent to the one we analyze here in which the offset of the voltage of electrode A is negative, and electrode B and C are grounded. It has been previously reported [28] that, in contrast to the results obtained with the sliding discharge, the application of a positive DC component to electrode C (or equivalently a negative DC to electrode A) has, for the same AC HV, a similar electrical power consumption than a classical DBD configuration.

Figure 4 shows the electrical power consumption P (mW/m) for the TED actuator considering several values of the absolute value of V_{DC}. While pure DBD configuration, ($V_{\mathrm{DC}} = 0$) consumes 565 mW/m, TED configuration show lower values of power consumption, with a minimum $P_{\min} = 398$ mW/m at around $V_{\mathrm{DC}} = 10$ kV. As we focus on results with $V_{\mathrm{DC}} = 11$ kV we can take $P_{\mathrm{TED}} = 425$ mW/m as a reference value.

3 Induced Electric Wind

In order to quantify the "electric wind" momentum that can be added to the flow, PIV measurements have been achieved in a low velocity configuration. The use of a low velocity flow, instead of quiescent air, allows to uniformize the seeding and minimize the effects associated with the electrical charging of the tracers. Tracers in proximity of the discharge region may acquire electrical charge by different mechanisms like for instance ion impact. Furthermore, momentum injection in a quiescent fluid environment may develop recirculation regions that tend to increase the presence of these charged tracers in the field of view of the experiment. Thus, PIV experiments performed in a quiescent environment may become contaminated by this effect as tracers may suffer an electrical force that is absent in the neighboring neutral fluid particles. The effect can be reduced by a suitable choice of tracers [1] but a small imposed flow allows a regular renewal of particles, helping to eliminate the recirculation regions

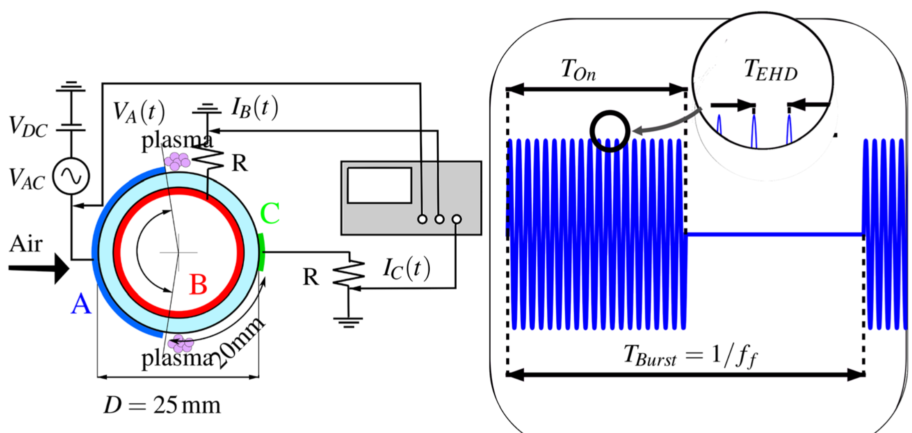

(*a*) (*b*)

Fig. 3 (*a*) Schematic and detail of the EHD actuator, electric circuit with the electrodes flush-mounted and (*b*) typical burst input waveform applied to the electrodes

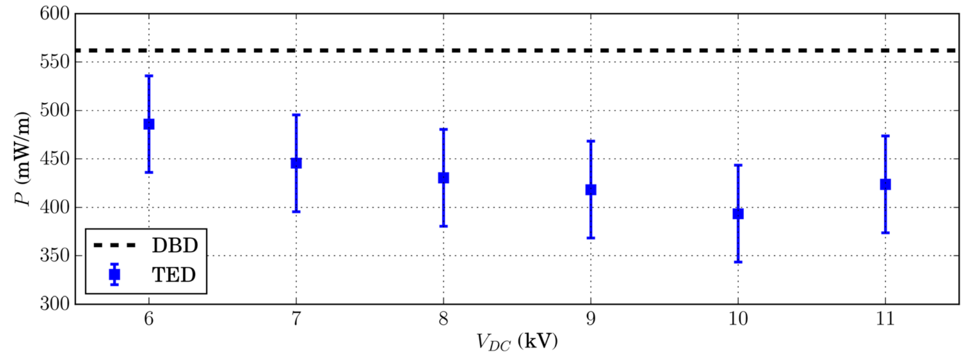

Fig. 4 Electrical power consumption for TED actuator (squares). Dotted line represents DBD actuator consumption.

and thus removing the charged tracers from the field of view of the experiment. In these measurements, a characteristic velocity $U_0 \simeq 0.24\,\mathrm{m/s}$ has been used ($\mathrm{Re} \simeq 400$), which is still considerably smaller than the values usually reported for DBD plasma actuators induced velocities, of the order of 2–5 m/s.

Figure 5(*a*) shows the mean velocity profiles at the downstream position $x/D = 4$ when this reduced free-stream velocity is imposed in the wind tunnel. The analysis of this figure reveals that the velocity profiles have a gaussian shape, that can be characterized by the maximum value V_j and a characteristic width b that we take equal to the distance between the maximum and the position associated to the standard deviation value.

The nondimensional momentum number $C_\mu = V_j^2 b/(U_0^2 D)$ can be used to compare the induced momentum by the electric wind against the characteristic momentum flux of the free stream when $U_0 = 3.3\,\mathrm{m/s}$ (or equivalently when the flow is at $\mathrm{Re} = 5500$). The results are summarized in Fig. 5(*b*) where we plot the induced momentum against the input voltage V_{DC}.

As Fig. 5(*b*) shows, and in agreement with the previous results [26], a strong induced momentum increment is observed when raising the absolute value of V_{DC}. Considering that in classical DBD devices the negative discharge (occurring during the negative half-cycle) produces a faster acceleration of the fluid than the positive one [28,32], it has been previously argued that the increase of induced momentum observed for the TED configuration is a consequence of a higher acceleration of the negative space charge created during the negative half-cycle.

4 Drag Forces

In this section, time-averaged drag forces are estimated from PIV velocity fields. The power savings from flow control compared to the power consumed by the EHD actuators are discussed.

4.1 Calculation of Forces With PIV. We have calculated the drag forces exerted by the flow on the cylinder from the velocity fields. There are different approaches to achieve this goal in the literature (see for instance [33]), and we consider one which principle consists in integrating both momentum budget in a control volume V and pressure forces on the corresponding boundary surface S

$$\mathbf{F}(t) = -\frac{\mathrm{D}}{\mathrm{D}t}\int_V \rho\mathbf{u}\,\mathrm{d}v + \int_S (-p\mathbf{I} + \mathbf{T})\cdot\mathbf{n}\,\mathrm{d}s \tag{3}$$

where $\mathbf{u}$ is the velocity field, ρ is the fluid density, p is the pressure field, $\mathbf{I}$ the unit tensor, $\mathbf{T} = \mu(\nabla\mathbf{u} + \nabla^{\mathrm{T}}\mathbf{u})$ is the viscous stress tensor, the viscosity μ and $\mathbf{n}$, a unitary vector field orthogonal to the boundary S. Neglecting the effect of inhomogeneities in the flow along the spanwise direction, the projection of time-averaged Eq. (3) in the streamwise direction yields

$$\langle F_D\rangle = -\rho\int_S \langle u_x\rangle\langle u_y\rangle \mathrm{d}s - \rho\int\int_S \langle u'_x u'_y\rangle \mathrm{d}s - \int\int_S \langle p\rangle \mathrm{d}s + \mu\int\int_S \frac{\partial\langle u_x\rangle}{\partial y}\frac{\langle\partial u_y\rangle}{\partial x}\mathrm{d}s \tag{4}$$

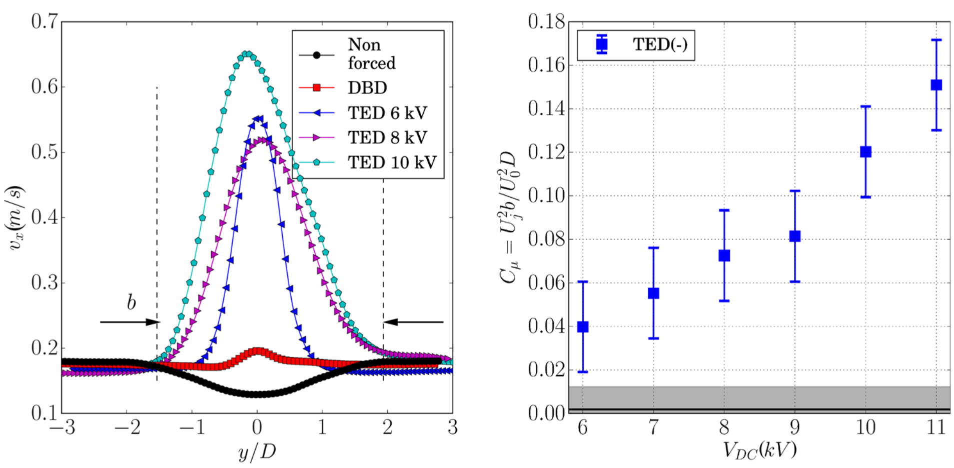

(*a*) (*b*)

Fig. 5 (*a*) Wake velocity profiles for nonforced and forced flow at $x = 4$, and (*b*) normalized momentum flux produced by TED actuators

ID: asme3b2server Time: 21:05 I Path: //chenas03/Cenpro/ApplicationFiles/Journals/ASME/FE##/Vol00000/170026/Comp/APPFile/AS-FE##170026

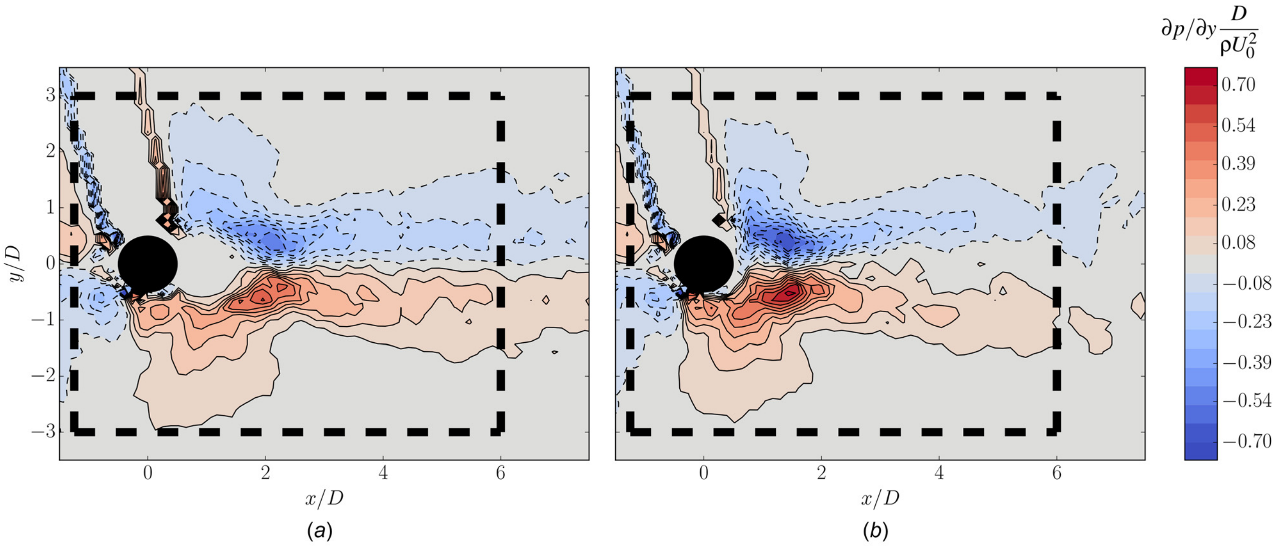

Fig. 6 Contour levels for the time-averaged *y*-component of pressure gradient $\langle \partial p/\partial y \rangle$ for nonforced flow (*a*) and under TED $V_{DC} = -11$ kV, $f^+ = 1$ (*b*). Dashed lines show control volume boundaries.

The main difficulty of this expression is the estimation of the pressure field from the 2D velocity field. This is achieved either by means of the Poisson equation (see e.g., Ref. [34]), or by integrating the Navier–Stokes (NS) equation along the control surface [35]. This latter idea has been refined by Kurtulus et al. [33]: the NS equation is integrated only in the wake region, while the Bernoulli equation is used in the slowly evolving potential flow region. Thus, obtaining the pressure p along a $s-$ curve is achieved by the following equations:

$$p(s) = p(s - \mathrm{d}s) + \nabla p \cdot \mathbf{ds}, \quad \text{on the downstream frontier} \tag{5}$$

$$p(s) = \partial \phi / \partial t + p_0 - \frac{1}{2}\rho |\langle \mathbf{u} \rangle|^2, \quad \text{otherwise} \tag{6}$$

where ϕ is a time invariant potential for the flow. The dominating term for the estimation of the force is the average $\partial \langle p \rangle / \partial y$ at the control volume boundary which is immersed in the wake. Those are displayed in Fig. 6, where unforced flow (*a*) is compared to TED forced flow (*b*) with $V_{DC} = -11$ kV, $C_\mu = 0.15$, and $f^+ = 1$.

For the unforced flow, $C_D = 2F_x/\rho U_0^2 DL \simeq 1.1$. Being this value in good agreement with the available experimental data of the literature (see for instance the values reported in Ref. [36] for $\mathrm{Re} = 5500$) we assume that the drag estimation strategy considered is adequate for our study.

In order to evaluate the measurement uncertainty, the estimation of C_D is obtained for 64 different boundaries for the control volume, dashed lines in Fig. 6, within $\pm 1D$ of the boundary used for the nominal C_D value. The standard deviation of these values are used as indication of the uncertainty and represented by error bars in Fig. 7.

Before exploring the effect of periodic forcing, stationary forcing is evaluated as a baseline case.

Figure 7 compares the evaluated drag force for the unforced flow, stationary DBD-actuated flow and stationary TED-actuated flow with increasing values for the negative DC voltage applied on electrode C.

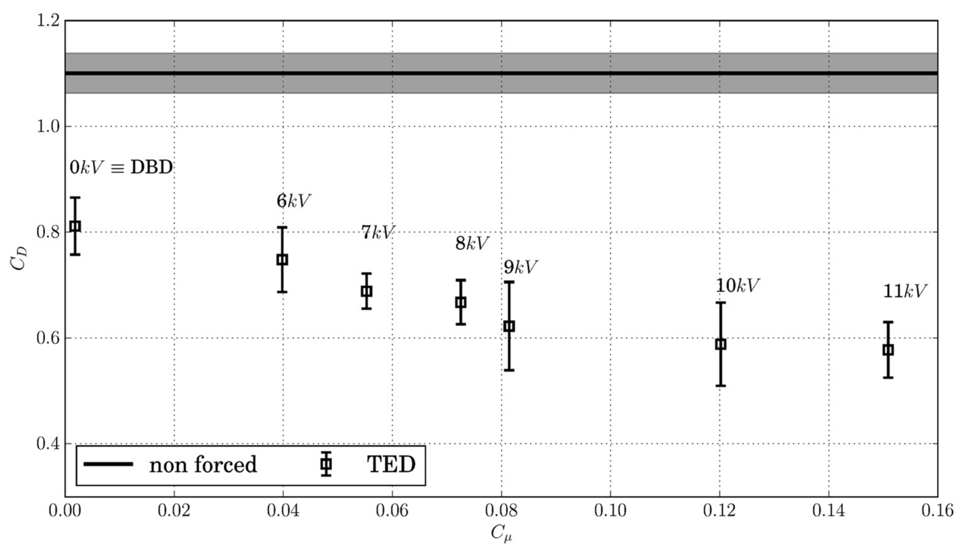

Fig. 7 Drag coefficient estimation for the unforced case (solid line), DBD and TED enhanced through stationary forcing mode. Electrode A DC voltage is decreased from 0 to −11 kV so nondimensional momentum C_μ increases monotonically with respect to V_{DC}.

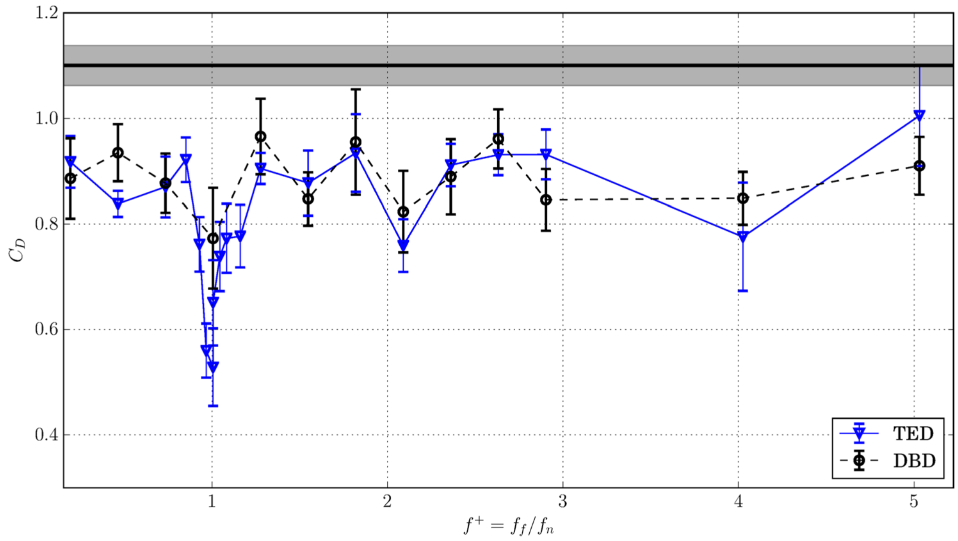

Fig. 8 Drag coefficient estimation for nonforced case, DBD and TED enhanced (−11 kV)) through harmonic forcing at DC = 50%. Forcing frequencies $f^+ = f_f/f_0$ are from 0.2 up to 5.0, measurements have been refined around the minimum at $f^+ = 1$.

Stationary DBD forcing produces a 20% drag reduction with respect to the natural case using the least favorable uncertainties. This is consistent with drag measurements reported in Refs. [17] and [26]. Negative voltage is then varied between −6 kv and 11 kv. As C_μ increases (Fig. 5(*b*)), C_D decreases almost linearly from a value close to the DBD-actuated flow (0.8) to $C_D \simeq 0.64$ at $C_\mu = 0.15$, when the electric field is the strongest at $V_{DC} = -11$ kV. The decrease of drag in our study is larger than the one reported in the previous experiments [26], but we associate this to difference in the experimental setup and electrode arrangement. Throughout the following results, TED measurements were performed imposing $V_{DC} = -11$ kV.

The fluctuations induced by Bénard–von Kármán absolute instability are natural targets for any control experiment on the cylinder flow. Hence, and as highlighted by the previous studies [17,20], it is reasonable to perturb the flow at frequencies close to the natural vortex shedding. Setting $V_{DC} = -11$ kV, periodic forcing is tested with both DBD and TED configurations for a duty cycle DC = 50% and $f^+ \in [0.2\ldots5]$. The corresponding drag coefficients are presented in Fig. 8. Contrary to Ref. [17], no increase of the drag is detected for DBD forcing frequencies close to the natural vortex shedding frequency. For both actuators (DBD and TED), a strong drag reduction near $f^+ = 1$ is obtained.

In order to better characterize this performance, the parametric study has been refined around this value. The global behavior is similar in both configurations: while drag reductions of about 10 or 20% are obtained for a number of cases, a dramatic decrease of C_D, up to 45% for TED at $f^+ = 1$, is observed. As for the other frequencies tested, the net C_D gain is rather constant and close to the DBD forcing case in opposition to the stationary blowing cases. Also, it can be noted a small decrease in C_D close to the first harmonic, with a 32% reduction.

The role of the duty cycle has been evaluated by varying its value from 6% to 50% and estimating the corresponding C_D with $f^+ = 1$. The corresponding drag coefficients are presented in Table 1. From a first evaluation of these values, large drag reductions are observed for DC as low as 31%. Energy savings are thus feasible, and this aspect is discuss in what follows.

Table 1 C_D varies at f^+=1 for duty cycle (DC) values between 6% and 50%

DC	6%	12%	19%	25%	31%	37%	44%	50%
C_D	0.98	0.80	0.66	0.67	0.57	0.60	0.57	0.56

4.2 Energy Efficiency. For DC values of the order of 20%, a good compromise between the performance (drag reductions of about 40%) and energy savings takes place. The power associated to drag for the nonforced flow can be roughly estimated as $P_D = F_D U_0 = \rho C_D U^3 DL/2 = 296$ mW (or equivalently power per spanwise unit length $P_D/\mathrm{m} = 592$ mW/m). Figure 4 shows a consumption of $P = 425$ mW/m for the TED actuator at DC = 100%, and this value reduces proportionally when reducing the DC.

The dissipated electric power, the reductions of power associated to drag forces, and the drag power savings are presented on Fig. 9 for a TED actuation and for the different values of DC per spanwise unit length. These powers are normalized with the power associated to the drag forces in the absence of actuation. Analyzing simultaneously Table 1 and Fig. 9(*a*) one can conclude for instance that TED enables for DC = 19% a drag reductions close to 40% accompanied by a net energy saving of 27%. There are other options to quantify net energy savings. Different authors have defined for instance coefficients named saving rates or power saving ratios depending on the flow-control application considered [37]. Jukes and Choi [18] defined an energy efficiency, η_e, to evaluate cylinder wake control with DBD actuation. This coefficient is defined as the ratio of the power saved by drag reduction $\Delta P_D = P_{D0} - P_D$ (with P_{D0} the power associated to drag when the flow is nonactuated) to the electrical power applied to the actuator, P_{TED}, measured from voltage and current waveforms: $\eta_e = \Delta P_D / P_{\mathrm{TED}}$. Note that using this definition values of η_e higher than one of this coefficient indicate a net energy saving that includes in the energy balance all the chains of efficiency to transform to mechanical power the electrical energy supplied to the actuator. From a thermodynamic point of view, only control systems with η_e higher than one are adequate. Jukes and Choi [18] found for similar Reynolds number that we consider in this manuscript, values of η_e of 0.51. It seems pertinent therefore to compare our results considering the same coefficient these have proposed. We show on Fig. 9(*b*) the values of η_e against DC. This graph illustrates that for DC = 19% an energy efficiency of 2.9 is attained, a value that is largely higher than those reported in Ref. [18]. This, however, is not surprising as these authors have already signaled in their manuscript that savings rate could be

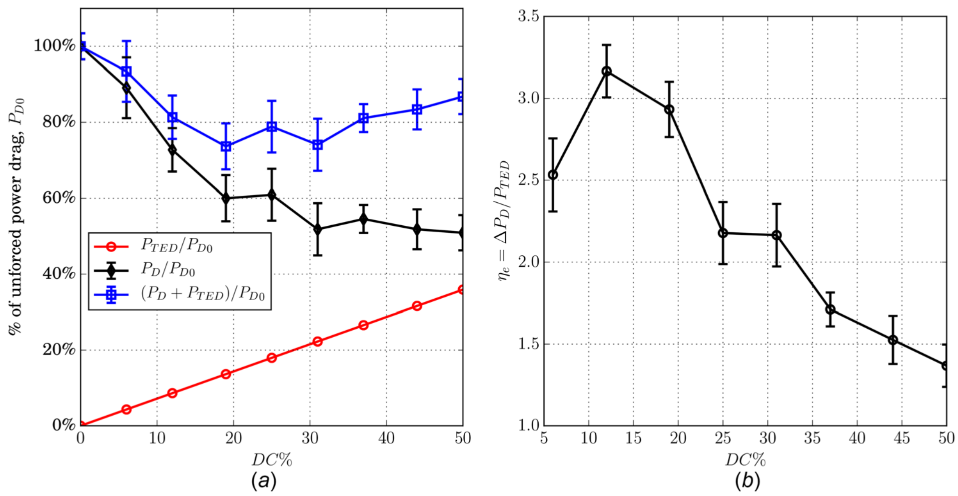

Fig. 9 (*a*) Electric power P_{TED}, drag dissipated power P_D and total lost power $P_{TED} + P_D$ as duty cycle D_C rises. Values are normalized with the power associated to drag forces when no actuation is imposed P_{D0}. A maximum 27% net energy saving can be achieved for a 19% duty cycle, still corresponding to a 40% drag reduction. (*b*) Energy efficiency versus duty cycle for TED actuation. In both figures Re = 5500 and $f^+ = 1$.

improved through the optimization of both actuator design high voltage power supply. To the best of our knowledge, this is the first work that reports a control strategy of a wake flow with energy efficiency larger than one. Note also that these high values of efficiency are accompanied simultaneously with an important drag reduction.

In the next paragraphs, we propose to disclose the underlying physical mechanisms associated to this actuation performance observing the time-averaged and dynamical properties of the flow fields.

5 Discussion on Drag and Wake Structures

In this section, we evaluate the flow dynamics modifications introduced by the actuator considering PIV measurements. First, we analyze mean flow and velocity fluctuations profiles in order to resume and quantify these modifications. Afterward, we reconstruct the vortex dynamics using a clustering technique.

5.1 Mean Flow and Global Modes. Stationary and harmonic forcing both produce mean flow modifications as evidenced in Fig. 10. Strong modifications of this field have associated alterations of principal coherent structures of the flow [38,39]. At the Reynolds number considered, the BvK vortex shedding remains the dominating flow structure, and for the unforced case, a recirculation region enclosing two counter-rotating vortices can be identified in the time-averaged flow field (Fig. 10(*a*)). It is possible to characterize this recirculation region with the recirculation length ℓ_m defined as the distance between the cylinder and the furthest downstream point belonging to a closed streamline. For the unforced flow, a value $\ell_m = 2.5D$ is found. When forcing is applied, the recirculation region is largely modified. This is illustrated with the mean flows of actuated cases displayed on Fig. 10(*b*) for DBD and Fig. 10(*c*) for TED. In both cases $f^+ = 1$ and $DC = 50\%$, and a strong decrease of the recirculation length of 1 to $1.5D$ (around 50% of ℓ_m) takes place.

This is accompanied by a narrowing of the wake and accelerations of the upstream shear layer region. This last effect is stronger with the TED actuator than with DBD as demonstrated by the time-averaged velocity profiles $\langle u_x \rangle$ in Fig. 11(*a*). Also further downstream, TED actuator produces a much lower momentum deficit than unforced or DBD-actuated flows.

The study of the average fluctuation profiles $\langle u_y'^2 \rangle^{1/2}$ (Fig. 11(*b*)), $\langle u_y'^2 \rangle^{1/2}$ (Fig. 11(*c*)), and $\langle u_x' u_y' \rangle^{1/2}$ (Fig. 11(*d*)) reveals that both TED and DBD actuated flows, reduce the momentum deficit. There, TED forcing presents the largest reductions, particularly on

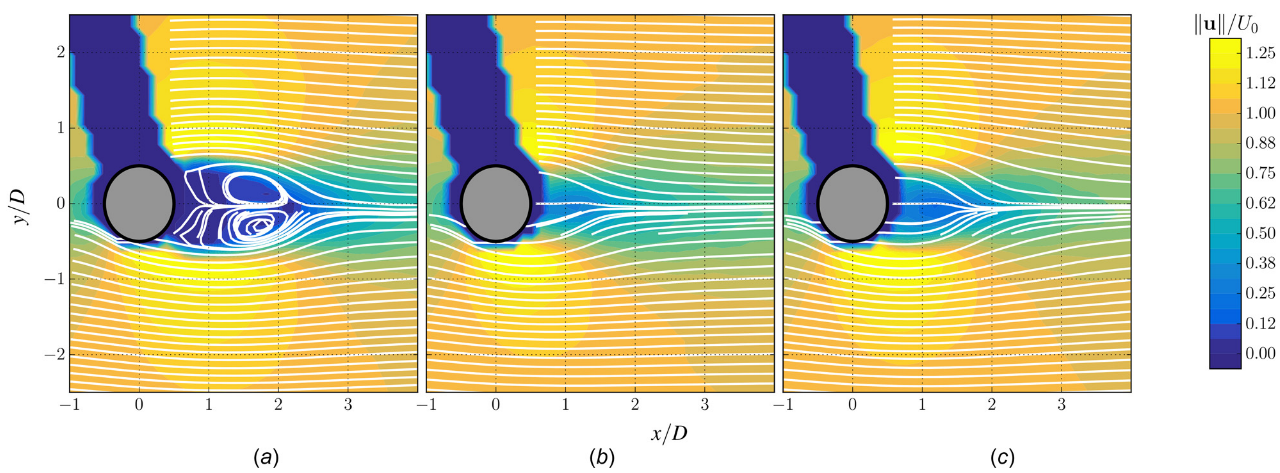

Fig. 10 (*a*) Mean flow streamlines and velocity modulus contours for Re = 5500, (*b*) DBD forcing at $f^+ = 1$, $DC = 50\%$, and (*c*) TED forcing at $f^+ = 1$, $DC = 50\%$

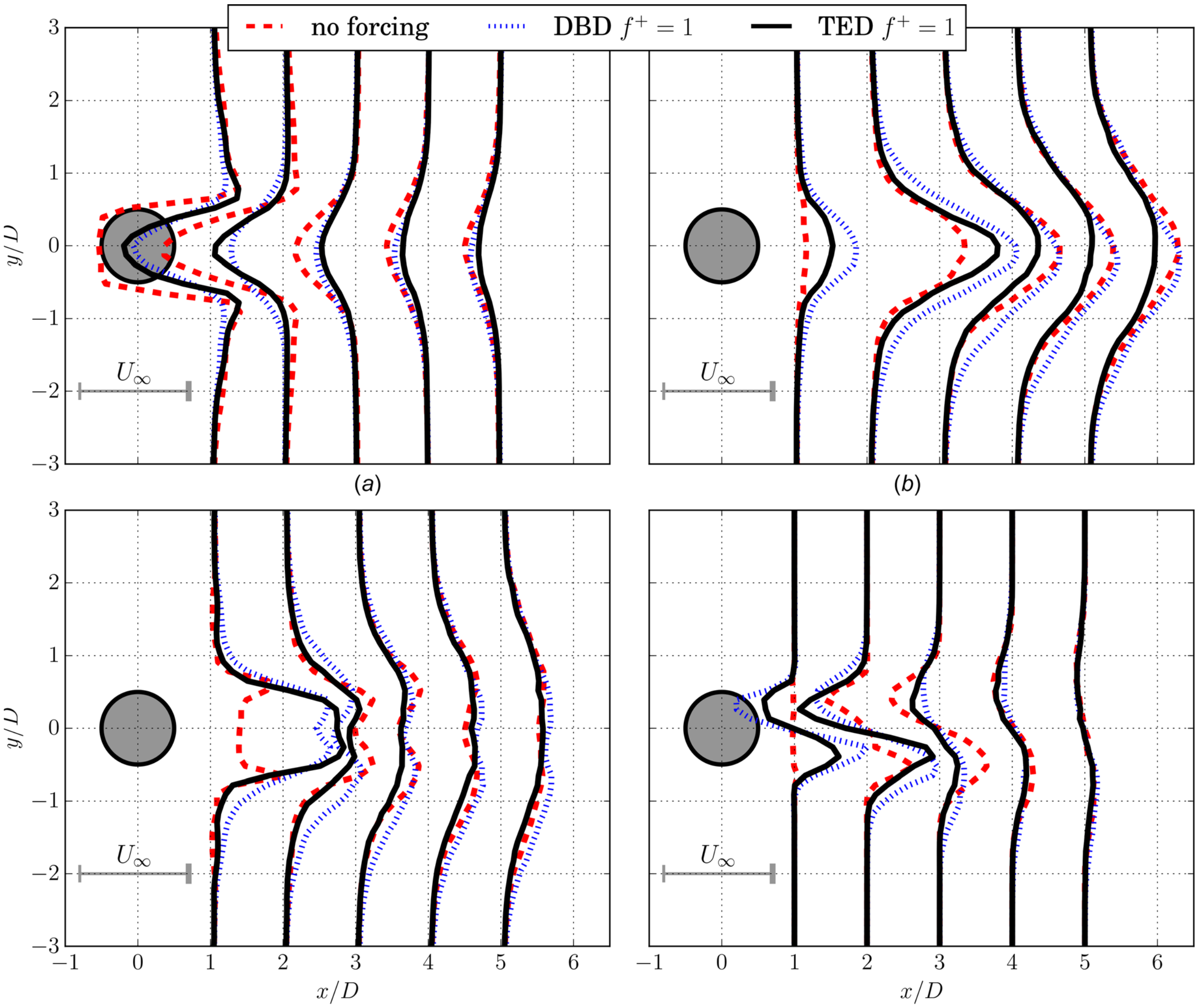

Fig. 11 Time-averaged velocity moments profiles: (*a*) $\langle u_x \rangle$, (*b*) $\langle u'y^2 \rangle^{1/2}$, (*c*) $\langle u'x^2 \rangle^{1/2}$, and (*d*) $\langle u'_x u'_y \rangle$. The profiles are taken at positions $x/D \in [1, 2, 3, 4, 5]$.

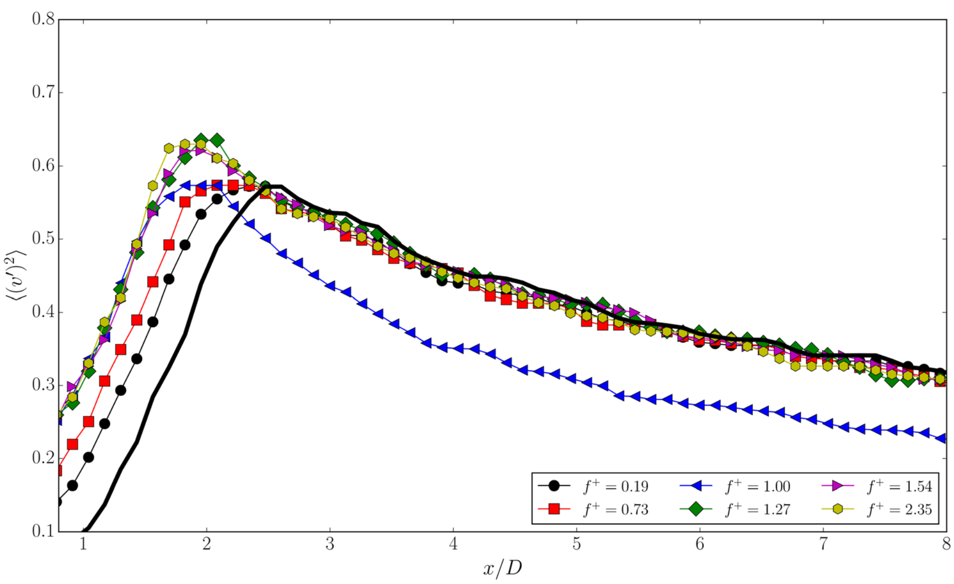

Fig. 12 Global mode shape modification under TED actuation for different forcing frequencies. The black thick line stands for global mode of the nonforced case.

$\langle u_y'^2\rangle^{1/2}$. As discussed in Refs. [40,41], this term is linked to the time-average pressure distribution in the wake $\langle p\rangle - p_0 = -\rho\langle u_y'^2\rangle$. The decrease in the fluctuations in the wake under both EHD actuations suggests a weakening of the intensity of vortex shedding in those configurations.

The dynamics of wake flows can be modeled considering them as a propagating wave, with an amplitude (determined by the fluctuating component of velocity) that grows from the origin, reaches a maximum and decays afterward. The spatial envelope of this coherent oscillation gives the amplitude of the so-called global mode (see e.g., Ref. [38]), for which the dominant contribution is given by the first harmonics. Figure 12 presents such global modes, taken as the profiles $\langle u_y'^2(y=0)\rangle^{1/2}$, for the unforced flow (solid black line) and TED actuated flows at different forcing frequencies. The unforced global mode reaches a maximum amplitude, about 0.57, at $x_M = 2.5D$, a value which is a measure of the vortex formation length [42] and quite comparable with the recirculation length ℓ_m. When the forcing frequency is $f^+ = 1$, then, $x_M \simeq 1.9$. The associated amplitude of fluctuations $\langle u_y'^2\rangle^{1/2}$ at the maxima is quite the same than the one observed the nonforced case. For higher forcing frequencies, $f^+ = 1.27; 1.54; 2.35$ the amplitude of the fluctuations is higher and attains values close to 0.64. We detailed, in the corner of Fig. 12, the behavior of the flow when the forcing frequency is around $f^+ = 1$. The global mode shape changes remarkably when f^+ is away from one.

It can be noted that in the context of rotatory oscillations [43,44], forcing at $f^+ = 1$ produces forced shedding modes locked to the absolute instability frequency. BvK structures are thus enhanced, and velocity fluctuations increase. On the contrary, the EHD actuators in the present study act symmetrically in both separating boundary layers. They introduce momentum at the same time at the cylinder wall and thus perturb the antisymmetrical natural vortex shedding process, decreasing the global mode amplitudes.

In Ref. [17], the authors indicate that an intermittent synchronized vortex shedding mode (Fig. 17 therein) may appear. The inspection of the instantaneous vorticity fields of DBD and TED cases of our study revealed in some cases the same type of vortex pattern these authors found. However, also classical BvK vortex structures were present in many snapshots. The acquisition frequency of the available PIV system (15 Hz) is below the natural frequency of the absolute instability (26 Hz for $\mathrm{St} = fD/U \simeq 0.2$), and thus, the dynamics of the flow was not time-resolved and no direct verification of the flow dynamics reported by Jukes and Choi [17] could be performed. In the next paragraph, we show a data treatment that gave us the opportunity to explore this aspect nonetheless.

5.2 Clustering Technique. As the dynamics of the flow could not be directly captured due to the low acquisition frequency, an indirect method was considered. For forced flows, a regular periodicity of the flow can be well established when lock-in regimes are attained. In the present work, even while the wake is periodically forced, the induced electric wind velocity is relatively small compared to the free flow velocity U and lock-in regimes are difficult to establish. Thus, instead of relying on

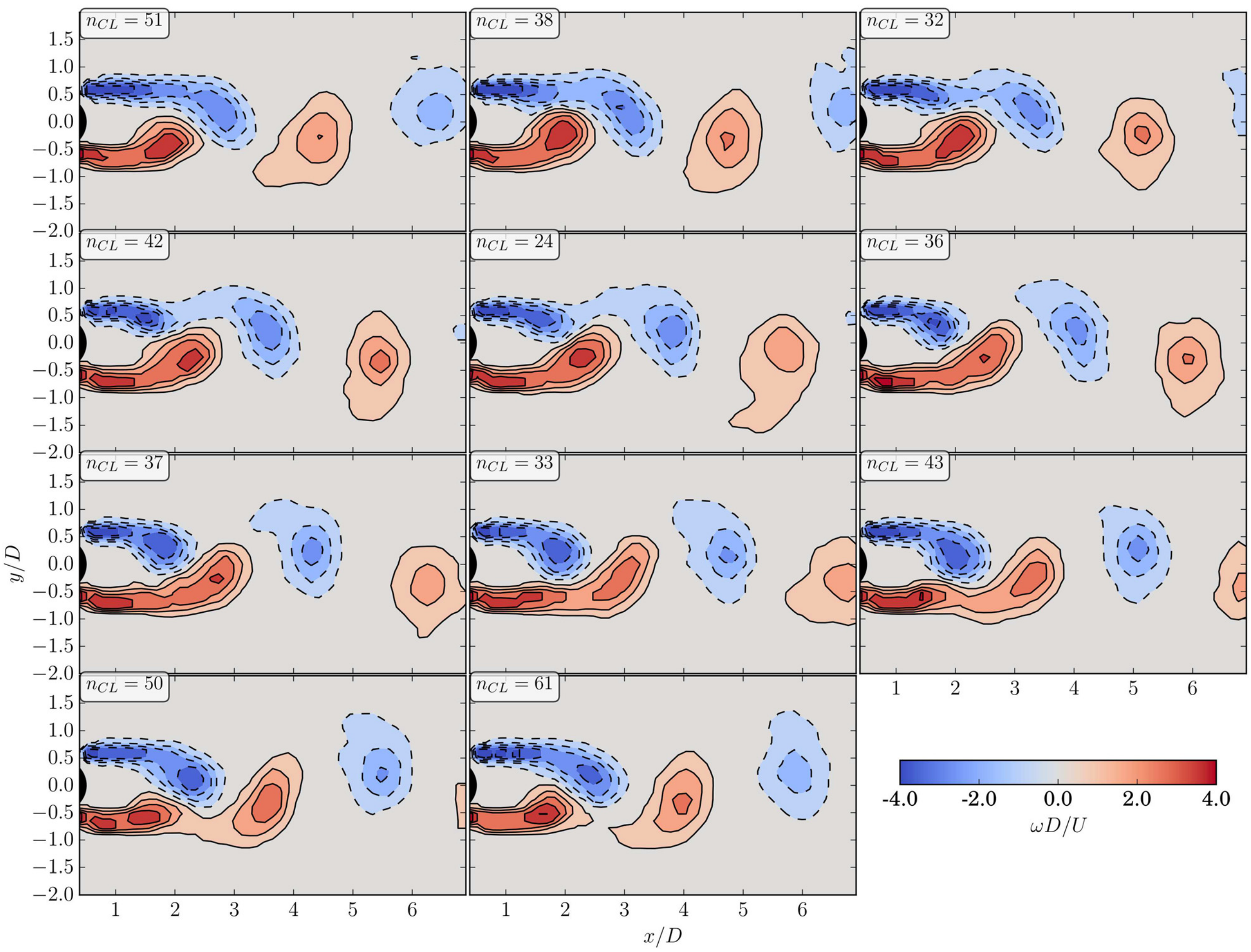

Fig. 13 For the nonforced flow, clusters portrait the vortex shedding dynamics from vorticity contour lines (solid for positive values and dashed for negative values) within one period. The number of snapshots involved is shown in each subplot; initial clusters are placed after the last one to complete the loop.

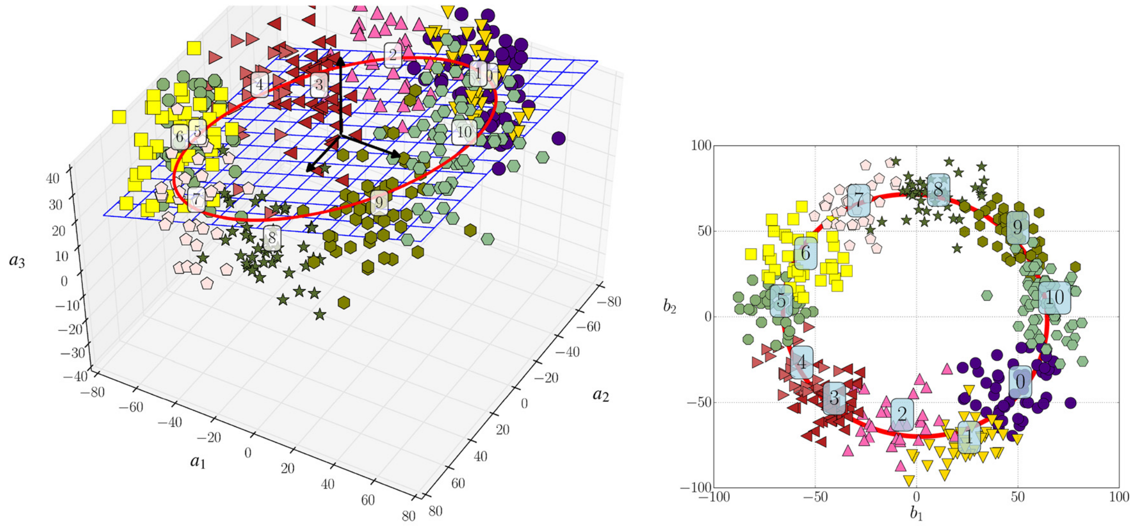

(*a*) (*b*)

Fig. 14 (*a*) Phase portrait from SVD of the vorticity clusters, three modes are enough to describe the dynamics of vortex shedding. A limit cycle attractor is emphasized by a minimum distance plane to the data, and a close curve that connects the centroids. (*b*) The result is clearer after a 2D projection onto the plane.

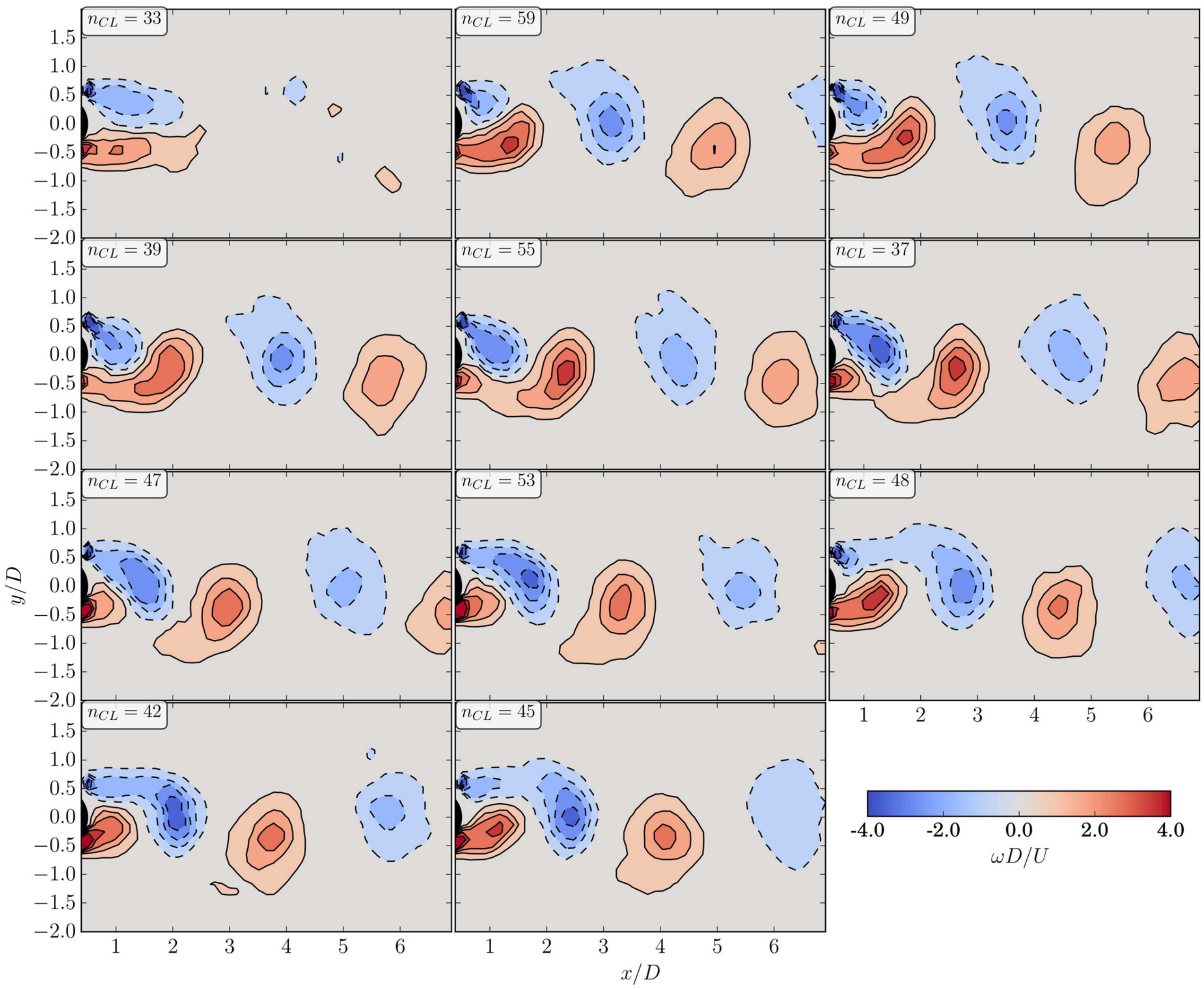

Fig. 15 Eleven clusters portrait the vortex shedding dynamics from vorticity contour lines within one period. The number of snapshots involved is shown in each subplot; initial clusters are placed after the last one to complete a loop. We observe two distinct regimes which correspond with BvK-like vortex shedding and two vortex sheets produced by DBD momentum injection.

simple-phase averaging techniques, a clustering technique, named *k*-means algorithm, was used to classify the acquired PIV fields and obtain a number of different representative states. This technique was introduced in the fluid mechanics community by Burkardt et al. [29]. Later, it was further developed by Kaiser et al. [45] to obtain the cluster-based reduced-order modeling (CROM) technique, that is, a statistical alternative to classical POD-Galerkin methods to obtain reduced-order empirical models. As time-resolution data are not available here, the full extent of CROM can not be used. Still the *k*-means clustering algorithm can be used to identify the different recurrent states of the coherent structures for this wake flow and their sequence.

The *k*-means algorithm [46,47] is a classification algorithm which aims at minimizing the average distance between a specified number N_c of points (called centroids) and the data in the phase space. Here, a point ω in the phase space representing one PIV snapshot is defined by the 3046 vorticity values obtained from said PIV snapshot in the spatial domain $x \in [1D\,6D]$, $y \in [-2D\,2D]$. Thus, the *i*th PIV field (out of 520 for each experiment) is defined by ω_i. The distance between two points is simply defined as the euclidean norm $\mathrm{d}(\omega_i, \omega_j) = \sqrt{\sum_{l=1}^{3046} (\omega_i(l) - \omega_j(l))^2}$.

The N_c centroids c_k, $k \in [1, N_c]$ are initialized with N_c random PIV fields. The following algorithm is then applied:

(1) the distance matrix D_i^k is constructed so that $D_i^k = \mathrm{d}(\omega_i, c_k)$.
(2) each snapshot ω_i is assigned to the centroid closer to its representation in the phase space.
(3) each centroid is displaced to the barycenter of the points representing its assigned snapshots.
(4) if no centroid is displaced, the method is stopped, otherwise it is iterated from Eq. (1).

When the method is stopped, N_c centroids are obtained, each one of them representing average states issued from the data and as separated as possible one from the other. A representation of a characteristic state of the flow can then be obtained by averaging all snapshots belonging to the same cluster. This method can be considered as a generalized phase averaging technique without the necessity of a strict periodicity of the phenomenon.

In this study, $N_c = 11$ clusters are used. This number is determined empirically by increasing N_c until the number of snapshot per cluster becomes statistically nonsignificant. The average vorticity field corresponding to each cluster is represented in Fig. 13 for the nonactuated flow.

As time resolution is not available, it is not possible to build the transition matrix that CROM uses to build a Markov's chain. Here, the order in which the clusters are explored by the flow can be deducted with the help of a cross-correlation between the centroids to build a chain of closest centroids. In Fig. 13, the clusters are ordered from top left (0) to right down (10), and the number of snapshots contributing to each cluster is displayed.

In order to reach a better description of this nonlinearly saturated oscillator, the 3046-dimensional data of the space phase is

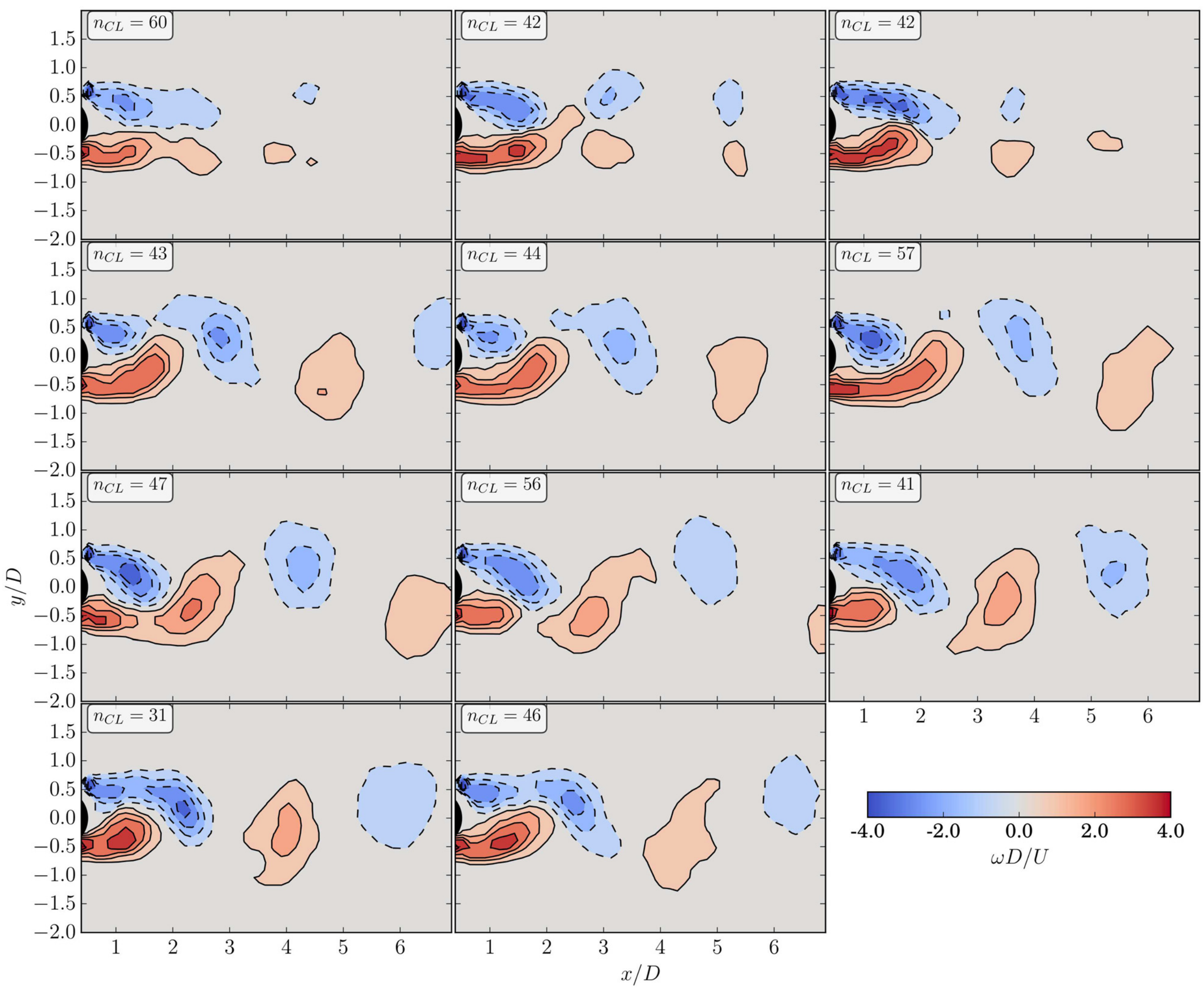

Fig. 16 ***Idem*** **Fig. 15 for TED momentum injection**

projected on three (respectively, two) dimensional subspace. The projection vectors are obtained using the three (respectively two) highest singular values of the correlation matrix of the clusters as described in Ref. [45]. In Fig. 14, every snapshot has been placed in the projection space, along with the centroids, indicated by their number. Snapshots belonging to the same cluster are in the same color. The resulting visualization displays the different snapshots placed close to a limit cycle indicated in red. This is coherent with the known behavior of the cylinder flow as a nonlinearly saturated oscillator limit cycle [39,48]. This kind of representation is close to what could be obtained with the first POD temporal modes [49].

Clustering technique is now applied to analyze the forced flow cases, particularly to those which present the optimum actuation to reduce drag forces on the cylinder. The contour levels for clusters that correspond to DBD configuration with a forcing frequency of $f^+ = 1$ are shown on Fig. 15. Remarkably, one of the clusters of the set cannot be easily included in a classic vortex shedding scenario. The cluster 0 (top, left) presents a symmetrical pattern with a distinct phase portrait than the others. The clusters 1–10 are asymmetric and display a BvK-like configuration in which formation and shedding of vortices are clearly near to the cylinder. Additionally, a similar scenario is found using the TED ($f^+ = 1$) as shown by the vorticity contour of each centroids on Fig. 16. In this case, the number of clusters with a symmetric-like vortex pattern increases (clusters 0,1,2), and BvK-like pattern develops in clusters 3–10.

Phase-space diagrams in Fig. 17 bring further light on these results. Figure 17(*a*) shows the 2D projection of the phase space for DBD actuation. BvK-like mode is distinctly observed with clusters centroids coherently connected, following the solid line, from 1 to 10. The symmetric pattern, cluster 0, is centered, equally distant from BvK modes trajectory. Similarly, TED forcing produces similar dynamical states which are represented in a more compact shape in the phase space of Fig. 17(*b*). Two distinct dynamical states are distinguishable: on one hand BvK-like mode from clusters 1 to 7 and on the other hand clusters 0,1,2 stand for symmetric vortex configuration.

There is a higher number of snapshots that belongs to the symmetric pattern with the use of TED, 28% of total, than with the use of DBD, 6%. TED forcing for this experimental setup therefore favors the formation of this symmetrical mode. This result is consistent with the observed improvements in drag reductions with TED actuation. A discussion on the link between vortex dynamics and forces in the wake flow is provided in the frame of the "impulse formula" presented by Saffman [50], $\mathbf{F} = -\mathrm{d}/\mathrm{d}t \int\int_S \mathbf{r} \times \omega dS$. An order of magnitude for the streamwise projection of the force in this expression can be obtained evaluating $\Xi = \int\int_S |y||\omega| dS$ in our clusters. In this sense, for nonforced flow, $\Xi \simeq 21$ for clusters in Fig. 13. On the other hand, TED controlled flow, Fig. 16 gives $\Xi \simeq 13$ (clusters 1 to 3) and $\Xi \simeq 18$ (clusters 4 to 11).

The larger recurrence of symmetric states can be thus associated to reductions of drag in wakes. This is in agreement with the theoretical results shown in Ref. [51] page 225, regarding vortex arrangements and their associated momentum in potential flow. Considering this approach, vortex symmetric configurations in a wake will produce a lower momentum deficit than asymmetric ones of the same intensity.

The symmetrical vorticity configuration has been observed by other researchers that have excited periodically the flow with symmetric forcings [52,53]. They have found that these patterns tend to occur when increasing the amplitudes of excitation.

In our work, the presence of symmetrical wake structures is more recurrent with TED actuation than for DBD, probably because TED produces stronger streamwise momentum. This is revealed by the larger proportion of snapshots where the flow shows a symmetrical structure.

Additionally, TED allows to control the size and position of the ionization region adjusting electrical parameters, and consequently, gives the possibility to tune the location of the resulting electrical force. This can be also done with DBD actuation but is restricted to a few millimeters. Therefore, TED is more versatile than DBD. DBD streamwise ionic wind may be also optimized through geometry modifications, i.e., moving downstream the position of the electrodes, but a similar effect is achieved just varying the voltage of the third electrode at the back stagnation point.

The statistical symmetrization of the wake is correlated with larger reductions of the drag associated to TED forcing. This can be explained in terms of alterations of the time-averaged flows and of velocity fluctuations. Recalling Sec. 4, Eq. (4), and Fig. 11, we can distinguish the terms that contribute to drag production. BvK-like mode promotes larger velocity fluctuations increasing the term $\rho\int\int_S \langle u'_x u'_y \rangle \mathrm{d}s$. Besides, these fluctuations decrease the pressure in the near wake producing a large pressure term $\int\int_S \langle p \rangle \mathrm{d}s$. Effectively, earlier studies show that the asymmetry of the vorticity accounts for a larger part of the drag [54] through a mean flow correction. A forcing that increases the recurrence of symmetric states therefore promotes larger reductions of drag. It has been also reported in the context of studies on propulsive wakes [40,41] that the average of the square of velocity fluctuations is linked to the pressure distribution in the wake. Hence, larger fluctuations produce larger deficits of pressure in the wake and in consequence larger drag forces. In our case, the vorticity fields of the clusters show a reduction of intensity for the actuated

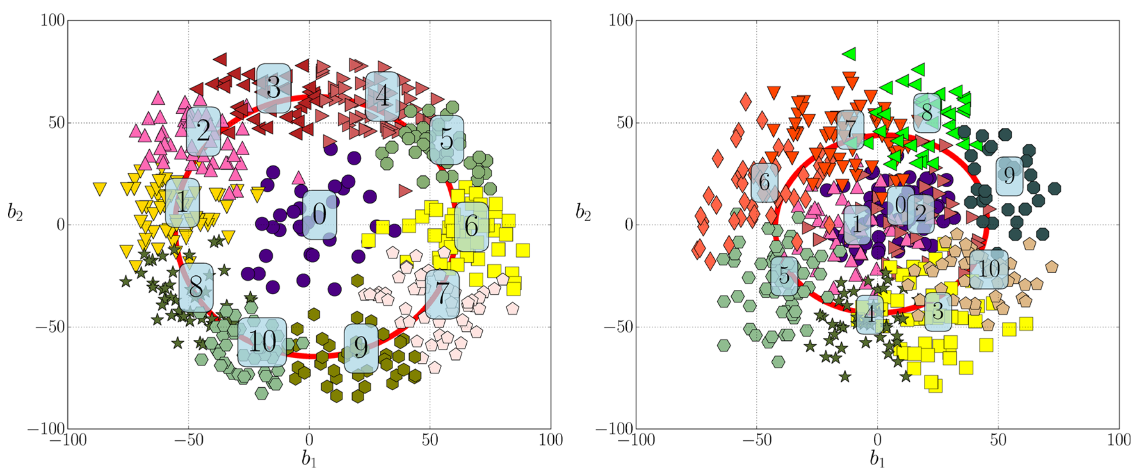

Fig. 17 Phase portrait from SVD of the vorticity clusters, three modes are enough to describe the dynamics of vortex shedding modified by actuation. Regimes identified in Fig. 16 correspond to the outer (BvK-like regime) or inner (TED momentum injection) phase space regions.

cases a phenomenon that is accompanied by simultaneous reductions of velocity fluctuations $\sqrt{\langle u_y'^2 \rangle}$ observed in Fig. 12. Therefore, the reduction of fluctuations we observe with the TED forcing is a desirable effect that contribute to reduce of drag.

6 Summary and Conclusions

Significant drag reductions, about 40%, can be achieved by means of forcing with TED actuators for the cylinder wake flow at Re = 5500. This has been obtained at the natural vortex shedding frequency $f^+ = 1$. Electrical power consumption was measured in order to quantify the cost of the control. The TED actuator at $f^+ = 1$, DC = 30% consumes the equivalent of 20% the drag energy loses, while it is able to reduce drag by 40%. Energy efficiency value for this case is as high as 2.22. The result suggests that TED actuation is a very efficient tool to govern the wake flow around cylinders in the Reynolds numbers range considered. Thus, it is a promising technique for flow control optimization for other Reynolds numbers and geometries. On one hand, for lower Re, the required induced momentum to produce symmetrical vorticity patterns should be smaller. So, the actuator should not have any issues to provide an efficient control. On the other hand, for higher Reynolds numbers, the limitation is given by the maximum induced velocity V_e that can be sustained by these actuators (∼10 m/s) compared to the free stream velocity U_0. As long as experiments remain in the shear layer transition regime ($10^3 < \mathrm{Re} < 2 \times 10^5$ [30]) and the ratio V_e/U_0 is not drastically changed, one would expect similar results. The interest of this work, however, does not restrict on reporting these outstanding characteristics of the performance of TED actuators but also on trying to explain the fluid physics associated.

Drag forces and a portrait of the wake fluid dynamics were estimated from a first analysis of PIV measurements. The focus was placed on harmonic forcing for values of the frequency in the neighborhood of the natural vortex shedding $f^+ \sim 1$. Significant modifications of the mean flow velocity fields were introduced by TED actuators with these forcing parameters.

It was observed through global modes analysis that minimum drag is achieved when transverse velocity fluctuations $\langle u_y'^2 \rangle$ are the smallest at $f^+ = 1$. As proposed by Raspa et al. [41], this result seems to corroborate that wake drag reductions occur when transverse momentum exchange is minimized. TED-induced flow produces a symmetric vortex configuration and lower fluctuations $\langle u_y'^2 \rangle$. This leads to a more favorable pressure distributions contributing to diminish drag forces especially when $f^+ = 1$. The high performance of the actuation is manifested when comparing this device to asymmetric ones, e.g., rotatory oscillations, in which only asymmetric vortex distribution can be reinforced by the actuation.

A clustering analysis with the experimental vorticity fields was performed in order to bring more support to the results. This tool enabled the reduction of the dynamics of coherent structures and also the classification of PIV snapshots. For the case in which TED forcing produces maximum drag reduction, clusters with asymmetric vorticity distributions (in a Bénard Von Kármán vortex like configuration) and clusters in which symmetry of vorticity fields prevails were identified. In the first kind of clusters, a shortening of the vortex detachment region is visible due to forcing. Additionally, as larger numbers of symmetric clusters are correlated to larger drag reductions, and it is worth mentioning that the symmetric vortex configuration plays a fundamental role on drag reduction.

Acknowledgment

The authors acknowledge grants of the CONICET and of the University of Buenos Aires.

Nomenclature

a_i = projection of ω onto POD $i-$ mode
b = characteristic width of the plasma-induced jet
b_1, b_2 = 2D projection of (a_1, a_2, a_3) POD modes
BvK = Bénard von Kármán
C_D = drag coefficient
C_μ = nondimensional momentum number
$d(\omega_i, \omega_j)$ = distance between PIV snapshots (i and j) for the flow vorticity
D = cylinder diameter
D_i^k = distance matrix
DBD = dielectric barrier discharge
DC = duty cycle for the electrical signal
DC% = electrical duty cycle
$\mathbf{F}$ = resultant force on the cylinder
f_n = natural vortex shedding frequency
f_S = sampling frequency
f_f = forcing frequency
F_D = drag force on the cylinder
f^+ = nondimensional forcing frequency
G = DBD induced flow rate
$\mathbf{I}$ = unit tensor
I_B, I_C = electric currents
L = cylinder length
ℓ_m = recirculation length
N = number of velocity fields snapshots
N_c = number of clusters
p = pressure
P = electrical power consumption
P_D = drag power associated to drag
P_{D0} = drag power associated to drag for the nonforced flow
P_{TED} = electrical power consumption for the TED actuator
PIV = particle Image velocimetry
Re = Reynolds number
s = curve coordinates
S = boundary surface for the control volume
St = Strouhal number
t = time
$\mathbf{T}$ = viscous stress tensor
t_i = time of a snapshot
T_{Burst} = forcing period by burst modulation
T_{Burst} = burst period to modulate the DBD signal
T_{On} = time during which the electrodes are energized
T_{ON} = time corresponding to DBD signal operating
T_{EHD} = period of the DBD signal
TED = three-electrode device
$\mathbf{u}$ = velocity field
u_j = j-component of the velocity field
$(u_j)'$ = fluctuations for the u_j component
U_0 = upstream free flow velocity
U_j = DBD induced jet velocity
ν = kinematic viscosity
V = control volume
V_J = maximum velocity value of the plasma-induced jet
$V_{\mathrm{AC}}, V_{\mathrm{DC}}$ = alternating, direct current voltagem, respectively
$\mathbf{x}$ = spatial coordinates
x, y, z = streamwise, transversal and spanwise spatial coordinates
x_M = position of the maximum amplitude for the global mode
x_M = position of the maximum amplitude for the global mode
ΔP = drag power saved by drag reduction
η_e = energy efficiency
ρ = density
ϕ = time invariant potential for the flow
ω = flow vorticity
ω_i = i-PIV snapshot for the flow vorticity
$\langle\rangle$ = time average operator

References

[1] Artana, G., D'Adamo, J., Leger, L., Moreau, E., and Touchard, G., 2002, "Flow Control With Electrohydrodynamic Actuators," AIAA J., **40**(9), pp. 1773–1779.

[2] Moreau, E., 2007, "Airflow Control by Non Thermal Plasma Actuators," J. Phys. D: Appl. Phys., **40**(3), pp. 605–636.

[3] Wang, J. J., Choi, K. S., Feng, L. H., Jukes, T. N., and Whalley, R. D., 2013, "Recent Developments in DBD Plasma Flow Control," Prog. Aerosp. Sci., **62**(■), pp. 52–78.

[4] Benard, N., and Moreau, E., 2010, "Capabilities of the Dielectric Barrier Discharge Plasma Actuator for Multi-Frequency Excitations," J. Phys. D: Appl. Phys., **43**(■), pp. 1–14.

[5] Bhattacharya, S., and Gregory, J. W., 2015, "Effect of Three-Dimensional Plasma Actuation on the Wake of a Circular Cylinder," AIAA J., **53**(4), pp. 958–967.

[6] Sosa, R., Grondona, D., Marquez, A., Artana, G., and Kelly, H., 2010, "On the Induced Gas Flow by a Trielectrode Plasma Curtain at Atmospheric Pressure," IEEE Trans. Ind. Appl., **46**(3), pp. 1132–1137.

[7] Corke, T., Enloe, C., and Wilkinson, S., 2010, "Dielectric Barrier Discharge Plasma Actuators for Flow Control," Annu. Rev. Fluid Mech., **42**(1), pp. 505–529.

[8] Duchmann, A., Simon, B., Tropea, C., and Grundmann, S., 2014, "Dielectric Barrier Discharge Plasma Actuators for in-Flight Transition Delay," AIAA J., **52**(2), pp. 358–367.

[9] D'Adamo, J., Sosa, R., and Artana, G., 2014, "Active Control of a Backward Facing Step Flow With Plasma Actuators," ASME J. Fluids Eng., **136**(12), p. 121105.

[10] Marks, C. R., Sondergaard, R., Wolff, M., and Anthony, R., 2013, "Experimental Comparison of DBD Plasma Actuators for Low Reynolds Number Separation Control," ASME J. Turbomach., **135**(1), p. 011024.

[11] Yang, L., Li, J., Cai, J., Wang, G., and Zhang, Z., 2016, "Lift Augmentation Based on Flap Deflection With Dielectric Barrier Discharge Plasma Flow Control Over Multi-Element Airfoils," ASME J. Fluids Eng., **138**(3), p. 031401.

[12] Rizzetta, D. P., and Visbal, M. R., 2012, "Plasma Control for a Maneuvering Low-Aspect-Ratio Wing at Low Reynolds Number," ASME J. Fluids Eng., **134**(12), p. 121104.

[13] Michelis, T., and Kotsonis, M., 2015, "Flow Control on a Transport Truck Side Mirror Using Plasma Actuators," ASME J. Fluids Eng., **137**(11), p. 111103.

[14] Artana, G., Desimone, G., and Touchard, G., 1999, "Study of the Changes in the Flow Around a Cylinder Caused by Electroconvection," Electrostatics 99, IOP Publishing Ltd, Bristol, Philadelphia, pp. 147–152.

[15] Artana, G., Sosa, R., Moreau, E., and Touchard, G., 2003, "Control of the Near-Wake Flow Around a Circular Cylinder With Electrohydrodynamic Actuators," Exp. Fluids, **35**(6), pp. 580–588.

[16] MacLaughin, T. E., Funska, M. D., Vaeth, J. P., Daulwalter, T. E., Goode, J. R., and Siegel, S. G., 2004, "Plasma-Based Actuators for Cylinder Wake Vortex Control," AIAA Meeting, Portland, Oregon.

[17] Jukes, T. N., and Choi, K. S., 2009, "Flow Control Around a Circular Cylinder Using Pulsed Dielectric Barrier Discharge Surface Plasma," Phys. Fluids, **21**(8), p. 084103.

[18] Jukes, T. N., and Choi, K.-S., 2009, "Long Lasting Modifications to Vortex Shedding Using a Short Plasma Excitation," Phys. Rev. Lett., **102**(25), p. 254501.

[19] D'Adamo, J., Gonzalez, L. M., Gronskis, A., and Artana, G., 2012, "The Scenario of Two-Dimensional Instabilities of the Cylinder Wake Under EHD Forcing: A Linear Stability Analysis," Fluid Dyn. Res., **44**(■), pp. 1–20.

[20] Benard, N., and Moreau, E., 2013, "Response of a Circular Cylinder Wake to a Symmetric Actuation by Non-Thermal Plasma Discharges," Exp. Fluids, **54**(2), pp. 1–19.

[21] Funaoka, S., Yamada, S., Ichikawa, S., and Ishikawa, H., 2014, "Interaction of Streamwise Vortex Pair Induced by Counter Type Plasma Jet With Flow Past a Circular Cylinder," J. Fluid Sci. Technol., **9**(3), pp. 1–8.

[22] Roth, J. R., 2003, "Aerodynamic Flow Acceleration Using Paraelectric and Peristaltic Electrohydrodynamic Effects of a One Atmosphere Uniform Glow Discharge Plasma," Phys. Plasmas, **10**(5), pp. 2117–2126.

[23] Berendt, A., Podliński, J., and Mizeraczyk, J., 2011, "Elongated DBD With Floating Interelectrodes for Actuators," Eur. Phys. J. Appl. Phys., **55**(1), p. 13804.

[24] Louste, C., Artana, G., Moreau, E., and Touchard, G., 2005, "Sliding Discharge in Air at Atmospheric Pressure: Electrical Properties," J. Electrost., **63**(■), pp. 615–620.

[25] Moreau, E., Louste, C., and Touchard, G., 2008, "Electric Wind Induced by Sliding Discharge in Air at Atmospheric Pressure," J. Electrost., **66**(1), pp. 107–114.

[26] Sosa, R., D'Adamo, J., and Artana, G., 2009, "Circular Cylinder Drag Reduction by Three-Electrode Plasma Actuators," J. Phys.: Conf. Ser., **166**(■), pp. 1–14.

[27] Benard, N., and Moreau, E., 2009, "Electric Wind Produced by a Surface Plasma Discharge Energized by a Burst Modulated High Voltage," 29th ICPIG, ■, Mexico, ■.

[28] Moreau, E., Sosa, R., and Artana, G., 2008, "Electric Wind Produced by Surface Plasma Actuators: A New Dielectric Barrier Discharge Based on a Three-Electrode Geometry," J. Phys. D: Appl. Phys, **41**(11), pp. 192–204.

[29] Burkardt, J., Gunzburger, M., and Lee, H. C., 2006, "POD and CVT-Based Reduced-Order Modeling of Navier-Stokes Flows," Comput. Methods Appl. Mech. Eng., **196**(1–3), pp. 337–355.

[30] Williamson, C. H. K., 1996, "Vortex Dynamics in the Cylinder Wake," Annu. Rev. Fluid Mech., **28**(1), pp. 477–539.

[31] Sosa, R., Arnaud, E., Memin, E., and Artana, G., 2009, "Study of the Flow Induced by a Sliding Discharge," IEEE Trans. Dielectr. Electr. Insul., **16**(2), pp. 305–311.

[32] Pons, J., Moreau, E., and Touchard, G., 2005, "Asymmetric Surface Dielectric Barrier Discharge in Air at Atmospheric Pressure: Electrical Properties and Induced Airflow Characteristics," J. Phys. D: Appl. Phys., **38**(19), pp. 3635–3642.

[33] Kurtulus, D. F., Scarano, F., and David, L., 2007, "Unsteady Aerodynamic Forces Estimation on a Square Cylinder by TR-PIV," Exp. Fluids, **42**(■), pp. 187–196.

[34] Fujisawa, N., Tanahashi, S., and Srinivas, K., 2005, "Evaluation of Pressure Field and Fluid Forces on a Circular Cylinder With and Without Rotational Oscillation Using Velocity Data From PIV Measurement," Meas. Sci. Technol., **16**(4), p. 989.

[35] Unal, M., Lin, J., and Rockwell, D., 1997, "Force Prediction by PIV Imaging: A Momentum-Based Approach," J. Fluids Struct., **11**(8), pp. 965–971.

[36] Delany, N. K., and Sorensen, N. E., 1953, "Low-Speed Drag of Cylinders of Various Shapes," Technical Report, NACA, Washington, DC, Report No. 3038.

[37] Kriegseis, J., Duchmann, A., Tropea, C., and Grundmann, S., 2013, "On the Classification of Dielectric Barrier Discharge Plasma Actuators: A Comprehensive Performance Evaluation Study," J. Appl. Phys., **114**(5), p. 053301.

[38] Wesfreid, J. E., Goujon Durand, S., and Zielinska, B., 1996, "Global Mode Behavior of the Streamwise Velocity in Wakes," J. Phys. II, **6**(■), pp. 1343–1357.

[39] Noack, B. R., Afanasiev, K., Morzynski, M., Tadmor, G., and Thiele, F., 2003, "A Hierarchy of Low-Dimensional Models for the Transient and Post-Transient Cylinder Wake," J. Fluid Mech., **497**(1), pp. 335–363.

[40] Raspa, V., Gaubert, C., and Thiria, B., 2012, "Manipulating Thrust Wakes: A Parallel With Biomimetic Propulsion," Europhys. Lett., **97**(■), pp. 1–5.

[41] Raspa, V., Godoy-Diana, R., and Thiria, B., 2013, "Topology-Induced Effect in Biomimetic Propulsive Wakes," J. Fluid Mech., **729**(■), pp. 377–387.

[42] Griffin, O. M., 1995, "A Note on Bluff Body Vortex Formation," J. Fluid Mech., **284**(2), pp. 217–224.

[43] Thiria, B., and Wesfreid, J. E., 2007, "Stability Properties of Forced Wakes," J. Fluid Mech., **579**(■), pp. 137–161.

[44] D'Adamo, J., Godoy-Diana, R., and Wesfreid, J. E., 2011, "Spatio-Temporal Spectral Analysis of a Forced Cylinder Wake," Phys. Rev. E, **84**(5), pp. 1–8.

[45] Kaiser, E., Noack, B., Cordier, L., Spohn, A., Segond, M., Abel, M., Daviller, G., Osth, J., Krajnović, S., and Niven, R. K., 2014, "Cluster-Based Reduced-Order Modelling of a Mixing Layer," J. Fluid Mech., **754**(9), pp. 365–414.

[46] Steinhaus, H., 1956, "Sur la Division des Corps matÃl'riels en Parties," Bull. lâĂŹAcadÃl'mie Pol. Sci, **IV**(12), pp. 801–804.

[47] Lloyd, S., 1982, "Least Squares Quantization in PCM," IEEE Trans. Inf. Theory, **28**(2), pp. 129–137.

[48] Provansal, M., Mathis, C., and Boyer, L., 1987, "Bénard-von Kármán Instability: Transient and Forced Regimes," J. Fluid Mech., **182**(1), pp. 1–22.

[49] Lumley, J. L., 1967, "The Structure of Inhomogeneous Turbulence," *Atmospheric Turbulence and Radio Wave Propagation*, ■, ■, pp. 166–178.

[50] Saffman, P. G., 1992, *Vortex Dynamics*, Cambridge University Press, ■.

[51] Lamb, H., 1932, *Hydrodynamics*, Cambridge University Press, ■.

[52] Williams, D. R., Mansy, H., and Amato, C., 1992, "The Response and Symmetry Properties of a Cylinder Wake Subjected to Localized Surface Excitation," J. Fluid Mech., **234**(■), pp. 71–96.

[53] Konstantinidis, E., and Balabani, S., 2007, "Symmetric Vortex Shedding in the Near Wake of a Circular Cylinder Due to Streamwise Perturbations," J. Fluids Struct., **23**(7), pp. 1047–1063.

[54] Protas, B., and Wesfreid, J. E., 2003, "On the Relation Between the Global Modes and the Spectra of Drag and Lift in Periodic Wake Flows," C. R. Mec., **331**(1), pp. 49–54.